Ceramics International xxx (xxxx) xxx

Contents lists available at ScienceDirect

Ceramics International

journal homepage: www.elsevier.com/locate/ceramint

Ultrafast high-temperature sintering of $BaCe_{0.65}Zr_{0.20}Y_{0.15}O_{3-\delta}$ electrolyte

Andrea Turino, Alberto Ferrario *, Stefano Fasolin, Jacopo Isopi, Filippo Agresti, Simona Barison, Stefano Boldrini

CNR—ICMATE, Institute of Condensed Matter Chemistry and Technologies for Energy, Corso Stati Uniti 4, I-35127, Padova, Italy

ARTICLE INFO

Handling Editor: Dr P. Vincenzini

Keywords:
Ultrafast high-temperature sintering (UHS)
Solid oxide electrolizer cells (SOECs)
BCZY
Clean energy
Proton conductor electrolyzer (PCE)

ABSTRACT

In recent years, ultra-fast high-temperature sintering (UHS) has gained increasing attention as a promising technique for the rapid synthesis and densification of a wide range of materials. UHS method allows to achieve high material density in a short time, while minimizing grain growth and volatilization of constituent elements. In this study, we present a simple method to sinter $BaCe_{0.65}Zr_{0.20}Y_{0.15}O_{3-\delta}$ (BCZY) electrolyte by UHS. The process enabled to obtain dense materials with relative densities above 95% within 20 s at a temperature up to 1550 °C. The overall energy consumption is in the Wh range, or tens of kJ g^{-1}. Sintered samples show good mechanical stability and high purity phase. Physical and electrochemical analyses were performed. Conductivity of 10.2 mS cm^{-1} at 700 °C is comparable with data from conventional sintering methods.

1. Introduction

To implement a hydrogen economy, a great effort is needed in the development of hydrogen production technologies, in particular water electrolysis combined with renewable sources. Among different electrolysis technologies, solid oxide electrolysis cell (SOEC) systems have excellent advantages such as high reaction rates and lower operating voltage compared to other technologies [1].

High protonic resistance of solid electrolyte at low temperature is the main issue to reduce operating temperatures of SOECs. Many ionic conductive materials have been explored so far, e.g., doped ZrO_2, CeO_2, $(La,Sr)GaO_3$, Bi_2O_3 [2–6].

Proton conducting SOECs, where the electrolyte is a proton conducting ceramic, are a valid alternative to reduce working temperatures. Among electrolytes investigated so far, Barium doped ceria resulted the most promising, for its compatibility to sulphur, the low activation energy and high proton conductivity in the temperature range 400–700 °C. In particular, the high conductivity of cerates and the chemical stability of zirconates can be combined in a solid solution between doped $BaCeO_3$ and $BaZrO_3$ [7,8]. Various solid solutions and dopants have been tested so far and 20% Zr and Y as dopant have been proved to have a good conductivity and chemical stability [8,9].

To obtain dense barium cerates ceramics, with low bulk and grain-boundary resistivities, high sintering temperatures, from 1400 °C to 1600 °C, for long time are required. However, it is known that prolonged exposition of the material to elevate temperatures causes BaO evaporation, which reduce concentration of oxygen vacancies and so conductivity [10]. Barison et al. proposed the 10mol% excess of Ba in $Ba_{1+x}Ce_{0.65}Zr_{0.20}Y_{0.15}O_{3-\delta}$ (BCZY) to overcome the barium deficiency [11]. Although Ba excess lead to higher sinterability and conductivity, in many cases unreacted BaO resulted in lower stability with respect to CO_2 [10,12]. More recently, Xu et al. proposed a microwave assisted sintering technique to lower the temperature to 1200 °C [13].

Moreover, conventional sintering, which normally requires tens of hour, is considerably energy demanding even at lower temperature. A recent sintering technique, Ultrafast High-Temperature Sintering (UHS) [14], can be the key for both energy saving and preventing loss of BaO. In fact, this technique consists in the rapid heating and cooling of the sample, within few tens of seconds, by means of Joule heating of graphite sheets. The sintering process features extremely fast heating rates and cooling (up to 10^3–10^5 °C min^{-1}) and high temperatures (up to 3000 °C). The technique has already proven to lead to dense pellets in tens of seconds with many materials like ceramics [15–20], metals [21], silicon nitride [22] and magnesium silicide for thermoelectric applications [23], to mention a few. Recently, Alemayehu et al. [24] used UHS technique to process gadolinia-ceria ceramic obtaining a density up to 95%. Pan et al. proposed a composite proton conductor composed of BZCY and LLZTO sintered through ultrafast high-temperature sintering [25]. An issue of UHS sintering often mentioned is the limited dimensions of sample which can be treated, however Zuo et al. [26]

* Corresponding author.
E-mail address: alberto.ferrario@cnr.it (A. Ferrario).

https://doi.org/10.1016/j.ceramint.2025.01.046
Received 20 November 2024; Received in revised form 13 December 2024; Accepted 3 January 2025
Available online 3 January 2025

proposed a new approach for the upscaling of UHS to consolidate large-sized ceramics. Finally, ultrafast high-temperature sintering could be applied to co-sinter multiple materials simultaneously, for fast material screening [14].

In this work, we take advantage of the UHS technique to sinter $BaCe_{0.65}Zr_{0.20}Y_{0.15}O_{3-\delta}$ prepared by sol-gel method without excess of Ba. We demonstrate that the developed process achieves full dense sample sintered in less than a minute, with very low energy consumption, and no appreciable Ba loss. A high conductivity in 200 °C–750 °C temperature range is reported, which is in good agreement with data of BCZY materials prepared by conventional sintering reported in literature.

2. Experimental

2.1. Powder synthesis

$BaCe_{0.65}Zr_{0.20}Y_{0.15}O_{3-\delta}$ powders were synthesized by using a sol-gel process based on a modified Pechini method [11]. The starting materials were $Ba(NO_3)_2$ (Sigma–Aldrich, 99+%), $Ce(NH_4)_2(NO_3)_6$ (Alfa Aesar, 99.5%), $ZrO(NO_3)_2{*}xH_2O$ (Alfa Aesar, 99.9 %), $Y(NO_3)_3{*}6H_2O$ (Alfa Aesar, 99.9%) as metal precursors, ethylenediaminetetraacetic acid (EDTA, Sigma–Aldrich, 99+%) as complexing agent and ethylene glycol (EG, Aldrich, 99+%) as polymerising agent. The water content of zirconium salt was determined by thermogravimetric analysis (TA-Instruments SDT-Q600). Ammonium hydroxide (Sigma Aldrich, NH_4OH sol. max 33%) was added to promote the dissolution of EDTA in deionised water (Millipore, Billerica MA, USA). A weighed amount of barium nitrate was firstly dissolved in deionised water at 80 °C, to obtain a total volume of about 80 ml. Hence, an aqueous solution of EDTA and ammonia (pH 9–10) was added dropwise to the barium solution (solution A, approximatively 120 ml). In a separate beaker, stoichiometric amount of cerium, zirconium and yttrium nitrate salts were dissolved in 50 ml of deionised water (solution B). The solution B was then added dropwise to the solution A to avoid irreversible precipitation.

The as obtained solution was then stirred overnight at 80 °C to ensure homogenization. After 20 h water was slowly evaporated resulting in a yellow–brown gel, also slowly dried at 140 °C. The dried gel was pyrolyzed in a two-step heat treatment at 300 °C and 550 °C in air, both for 3 h. The temperatures of the thermal treatments were chosen based upon thermogravimetric analyses as reported in our previous work [27]. The as obtained precursor powders were calcined in air at 1150 °C for 6 h. Final powders were characterized and used to obtain green pellets.

2.2. Sintering

Custom-built setup for UHS process consists of two 200 μm thick graphite sheets (TGP-H-60, Toray) with a heating area of about 20 × 15 mm^2 (20 mm electrode distance, 15 × 0.2 mm^2 cross-section) clamped between ceramic and copper plates. Copper plates are connected to a DC power source (1900B, BK precision). Two reflective metal shields, over and below graphite sheets, were used to uniform the temperature. The setup was inserted in a vacuum chamber. To perform a calibration, an S-type thermocouple is placed between the graphite foils in place of the sample. Metal shielded thermocouples have been shown to strongly disrupt the system, resulting in temperature underestimation [28]. An unshielded thermocouple insulated with a small alumina tube was employed to limit heat loss by conduction. Hence, the calibration was used instead of direct measurement to avoid thermal gradient in the sample and an inaccurate temperature assessment from an incorrect position. From repeated measurements, an uncertainty of several tens of degree should be taken into account. From the calibration curve an applied power range of 550–650 W was chosen to set the experiment temperatures near and above the conventional sintering temperature.

BCZY calcined powders were uniaxially pressed (400 MPa, 1 min) into pellets with size of 2 x 1 × 13 mm^3, which are suitable for electrical measurements. Pellets were inserted between the graphite foils, then the chamber was evacuated and filled with Ar. Joule heating of the graphite foils was performed by applying a DC current in the 50–60 A range in different experiments. In preliminary tests, a single step current profile leaded to a non-precise temperature control, due to current spikes, and possible cracks in the sample, as also reported in Refs. [24,29]. Hence, a staircase current profile of 1 A s^{-1} for 10 s was settled for heating and cooling, as shown in Fig. 1a. Consequently, a very fast initial heating rate was detected, >200 °C s^{-1}, and a subsequent slower increase up to the final temperature. Fig. 1b shows typical temperature profile and overall energy used. The staircase current profile resulted sufficiently optimized to be effective in densifying and avoiding current spikes and samples cracks. Overall sintering process requires 40 s.

Conventional sintering was also performed in a muffle furnace with the following setting: initial ramp from room temperature to 1450 °C (rate 2 °C/min), 10 h isotherm and passive cool down. So obtained sample was compared to UHS-processed ones.

2.3. Characterizations

The structural phase in powders and sintered pellets were evaluated by means of X-ray Diffraction (XRD) Analyses were carried out using a Panalytical Empyrean instrument, equipped with a Cu tube (Cu LFF HR – Kα1 = 1.540598 Å) operating at 40 kV and 40 mA. A rotating sample holder was used. Scans were performed in the range between 20 and 100°, at room temperature, with 0.05° per steps. Crystallite size and constituent phases were evaluated through Rietveld refinement and Maud software.

To evaluate structure and morphology, powders and sintered bodies were analyzed by Field Emission Scanning Electron Microscope and Energy Dispersive X-Ray Spectroscopy (SEM-EDS), with a Sigma Zeiss instrument (Carl Zeiss SMT Ltd., UK), and EDS Oxford Instrument.

Linear shrinkage and conventional sintering stages were evaluated by means of dilatometric measures (Netzsch DIL 402 PC), in the range 30 °C–1520 °C using a 5 °C/min heating rate and followed by a 30 min isothermal stage. Results were evaluated by means of Netzsch Proteus software.

Evaluation of density of sintered pellets was carried out by means of Archimedes' principle. Relative density was determined using a theoretical density value of 6.19 g cm^{-3} calculated from crystal lattice parameters measurements by XRD.

For electrical measurements Pt electrodes were sputtered onto each side of the pellets. Electrochemical Impedance Spectroscopy (EIS) characterizations of Pt\BCZY\Pt samples were carried out with GAMRY 600 Reference potentiostat in a two-electrode four-wire mode in the frequency range of 1 MHz–0.1 Hz, with an input signal of 50 mVrms. Measurements were recorded from 100 °C to 750 °C every 50 °C with a stabilization time of 20 min, in wet 5% H_2/Ar atmosphere. EIS measurements in 100 °C–250 °C range were carried out to investigate bulk and grain-boundary contributions. Impedance spectra were fitted with a double constant phase element/resistance parallel equivalent circuit to model bulk and grain boundary contributions.

3. Results and discussion

3.1. Microstructure

To obtain good density and mechanical stability, various preliminary experiments were performed with increasing final applied current, and consequent temperature. Current staircase and heating rate were the same. With a temperature lower than 1400 °C, i.e. with a power less than 600 W, non-considerable shrinkage was observed, and a very porous material was obtained with a density of about 79% (Fig. 2b). Conversely, with 20 s of holding time at a temperature of 1550 °C as per calibration a density of about 95% was reached. The temperature reached is slightly higher than that of conventional sintering. As suggested by Ref. [17], a

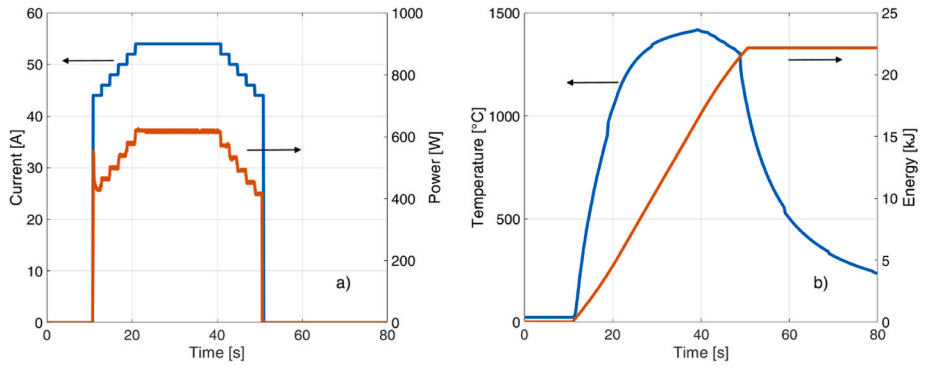

Fig. 1. a) Typical staircase current profile applied to graphite foils and resulting power. b) Temperature profile and total energy used during sintering process.

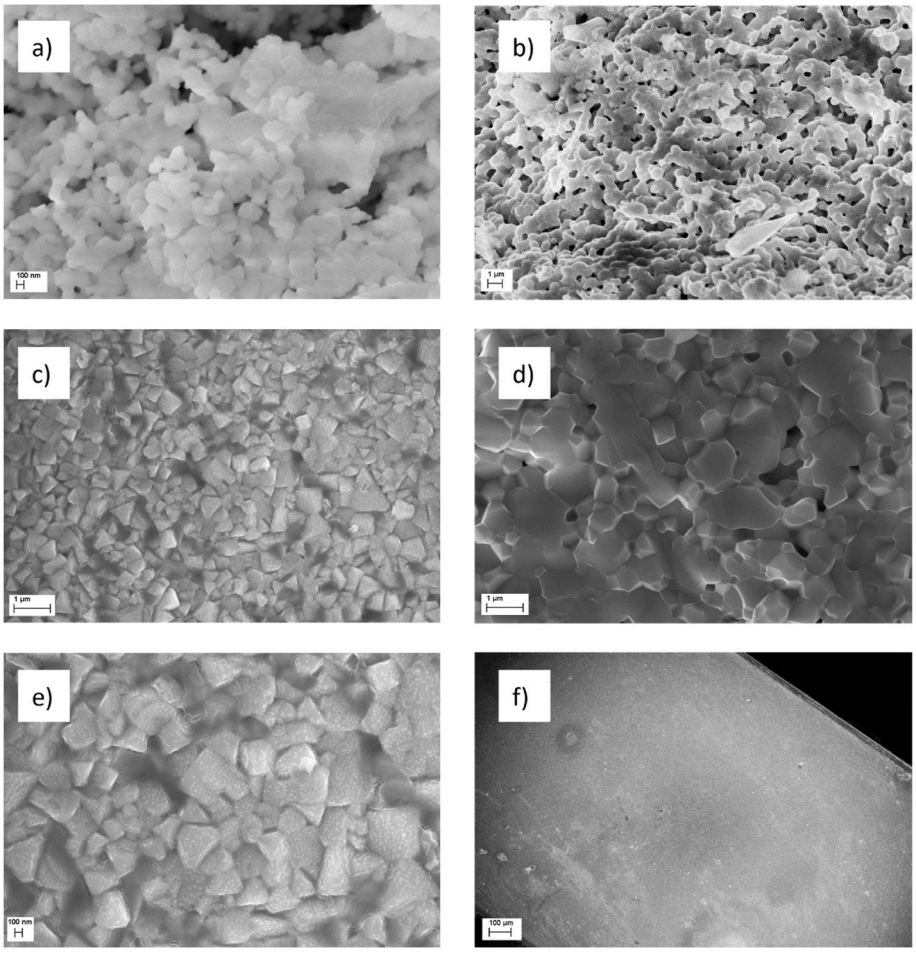

Fig. 2. a) SEM images of BCZY powder. Images of b) low density UHS-processed sample (1400 °C, 20 s) and (c, e) full dense BCZY UHS-processed samples obtained at 1550 °C for 20 s. d) Conventional sintered BCZY sample (1450 °C, 10 h). f) Overall appearance of the full dense UHS-processed sample (1550 °C, 20 s).

high heating rate requires a higher densification temperature. Similar findings are in Refs. [15,22,23]. SEM images, shown in Fig. 2c, confirm the densification of grains. Besides, SEM image over a large area of the sample shows that no cracks are evident, and sample is overall uniform (Fig. 2f), proving the reliability of the obtained temperature profile. As obtained UHS-processed sample was considered for conductivity measurements.

Noticeably, grain coarsening after UHS is limited if compared with starting powder (Fig. 2a), and the mean grain size of about 350 nm (Fig. 2c and e). For comparison, microstructure of conventionally sintered sample is reported in Fig. 2d, showing grains with a mean size of 700 nm. Hence, analyses confirmed that Ultra High-temperature Sintering promoted densification over grain growth.

3.2. Composition

XRD analyses and Rietveld refinement confirmed the correct phase of UHS-processed material. In particular, no Ba deficiency was detected, confirming that UHS, exploiting high heating rate and short treatment time, is effective in avoiding element evaporation.

Results of Rietveld refinement of XRD spectra (Fig. 3) are summarized in Table 1 for starting powder, sample obtained with conventional

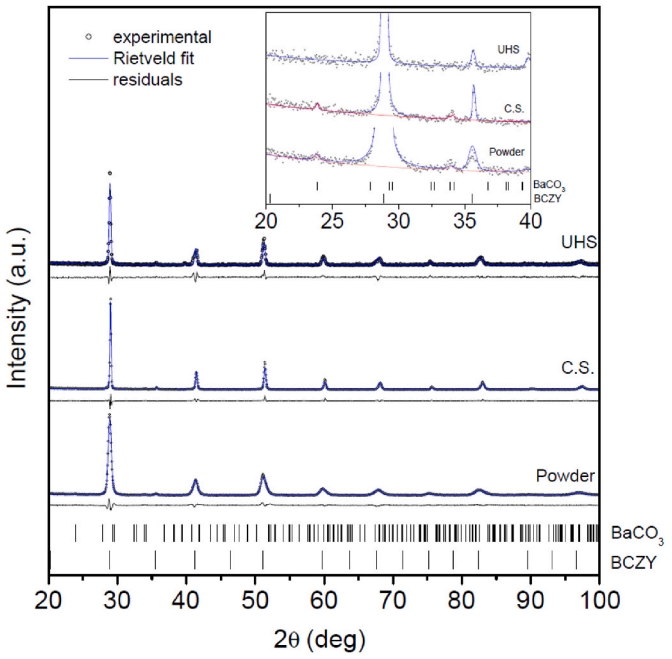

Fig. 3. XRD pattern of BCZY UHS-processed sample compared to starting powder and conventional sintered (C.S.) sample.

sintering and UHS. The as prepared powder shows the presence of a cubic BCZY with space group Pm-3m in accordance with [30,31]. A slight amount, less than 1 wt%, of barium carbonate was also detected. The microstructure is characterized by a crystal size around 50 nm and a moderate microstrain of 0.00562. The conventional sintered sample shows the same phases, with almost unchanged abundances. The cell parameter is 0.3% contracted with respect to the starting material, while the sintering process leads to a less defective microstructure with a substantial increase of crystal size up to almost 300 nm and a reduction of microstrain of 66%. Differently, sample obtained with UHS shows a lower increase of crystal size, which results about the half of conventional sintered sample (about 142 nm) whereas the main BCZY phase was confirmed. BCZY phase has relatively small microstrains, around 0.002. The measured UHS-processed sample shows no amount of barium carbonate, as indicated from the absent of $BaCO_3$ peaks in the inset of Fig. 3.

3.3. Impedance spectroscopy analysis

Electrochemical impedance spectroscopy was performed under wet H_2/Ar atmosphere to measure protonic conductivity of full dense BCZY UHS-processed pellet. Typical Nyquist plot of proton conductivity EIS measurements comprises two semicircles related to grain boundary resistance at low frequency and to bulk resistance at low frequency; additionally, a further arc at lower frequencies is attributed to electrode response. Representative impedance spectra of BCZY electrolyte recorded at 350 °C, 500 °C and 700 °C are shown in Fig. 4 together with corresponding fit. From the fitting, the low frequency semicircles give a capacitance between 10^{-5}-10^{-6} F, which can be ascribed to the electrode. On the other hand, the first semicircles show a capacitance in the 10^{-10} F range, responding for grain boundary contribution. Confirming this, at high temperature the grain boundary semicircle tends to disappear, and at operating temperature of fuel cell the main contribution to the conductivity is expected to be the bulk resistance [10], because the activation energy for transport through grain boundaries is higher than that for bulk. While increasing temperature, both semicircles shrink, meaning grain boundary resistance decreases. Even if it cannot be directly extrapolated at these temperatures, also the bulk resistance is shown to reduce. As expected, the overall conductivity, constituted of both bulk and grain boundary conductivities, increases of one order of magnitude from 350 °C to 500 °C, specifically from 2.8 10^{-4} S cm^{-1} to 2.6 10^{-3} S cm^{-1}. Then further increases to 1.02 10^{-2} S cm^{-1} at 700 °C.

Fig. 5 shows the 1000/T conductivity dependence of UHS-processed sample in wet H_2/Ar. From the Arrhenius plot the activation energy is calculate using:

$$\sigma = \frac{A}{T} e^{-\frac{E_a}{kT}}$$

where σ is the total proton conductivity, A is a preexponential factor, T is the temperature, k denotes the Boltzmann constant, and E_a denotes the activation energy of the conduction mechanism. The first sequence of impedance measurements shows an overall conductivity which is one order of magnitude lower with respect to following measurements, until 450 °C–500 °C. It is well reported that protonic conductivity in BCZY is promoted in moist atmosphere, hence the low overall conductivity and apparent higher activation energy can be addressed to an initial poor hydration of the sample at low moist atmosphere [7,9,32]. In fact, a

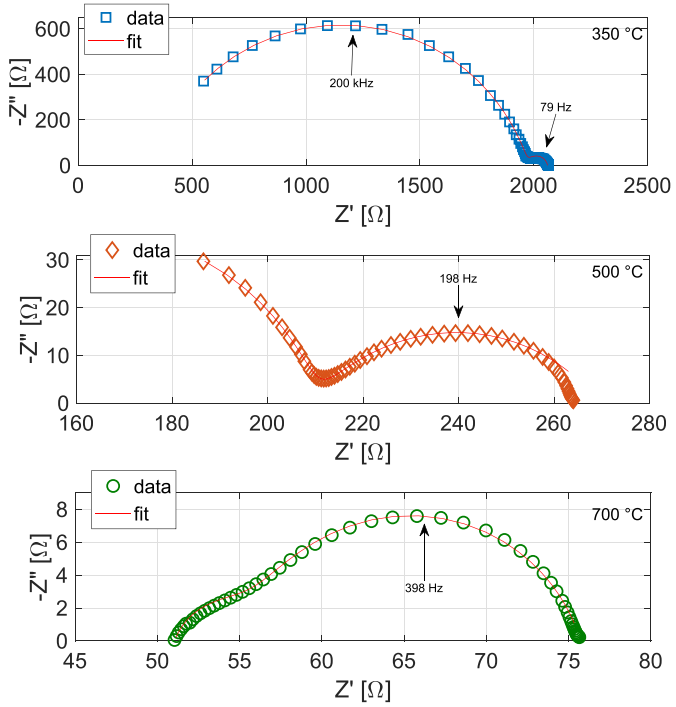

Fig. 4. Nyquist plots of impedance spectra of BCZY UHS-processed sample at three different temperatures measured in wet H_2/Ar. Arrows point the characteristic frequency of each arc. Solid lines represent fit to data with equivalent circuit.

Table 1
Microstructure comparison of starting powders and samples obtained with conventional sintering (C.S.) and ultrafast high-temperature sintering (UHS).

Title	Phase	wt%	a (A)	Size (A)	Microstrain	Phase	wt%	X^2
Powders	BCZY	>98	4.367	560	0.0056	$BaCO_3$	<2	1.8
Conventional sintering (C.S.)	BCZY	>98	4.352	2960	0.0019	$BaCO_3$	<2	1.6
Ultrafast High-temperature Sintering (UHS)	BCZY	100	4.361	1420	0.0028	–	–	1.3

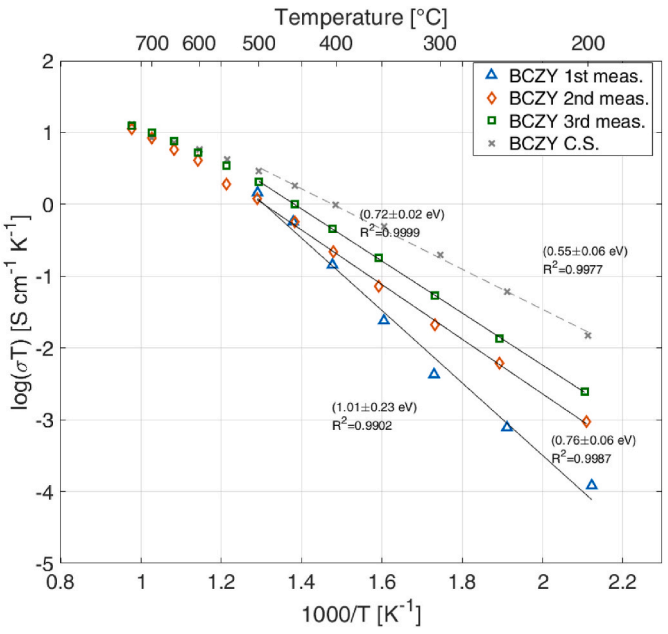

Fig. 5. Arrhenius plot of three consecutive measurement cycles of BCZY UHS-processed sample in wet H_2/Ar and comparison with conventional sintered sample. Solid lines represent linear regression to calculate the activation energy.

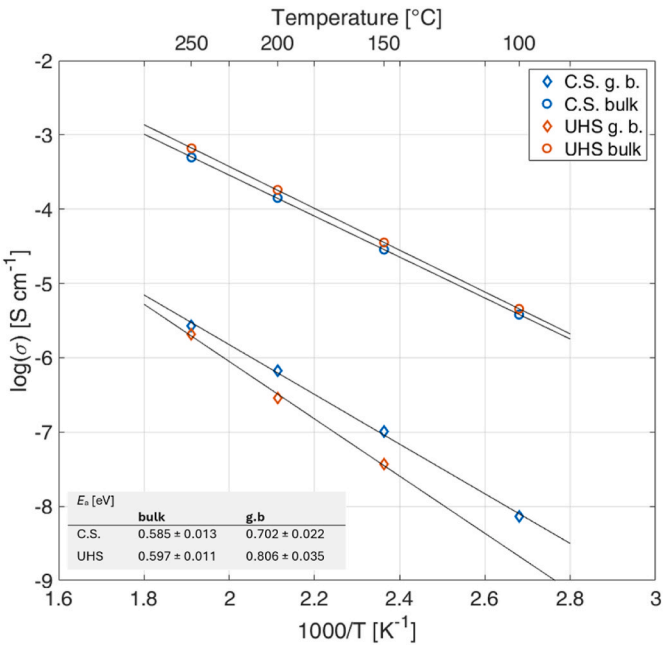

Fig. 6. Grain boundary and bulk conductivities of BCZY sample sintered with Ultrafast High-temperature sintering (UHS) and conventional sintering (C.S.). Solid lines represent linear regression of data. Activation energies for the transport of bulk and grain boundary are reported in the inset table.

large response in bulk conductivity to the change in atmosphere is reported.

Overall conductivity of UHS-processed sample stabilized with the third cycle of measurements, even if the second cycle curve is almost overlapping at high temperature and the activation energy results nearly the same.

A slope deviation at 550 °C was observed, which is also reported in Refs. [11,12] in wet H_2/Ar. Haile et al. [10] reported that an increase in grain size leads to a lower grain boundary resistance, and thus a higher total conductivity, simply because fewer boundaries are encountered by the mobile charge carriers. Likewise, higher conductivity of conventional sintered sample, in the lower temperature region, can be ascribed to the bigger grain size as shown by SEM analyses (Fig. 2), and to the lowest grain boundary resistivity as indicated by impedance analyses. Conductivities become almost identical in the PCE operating temperature range.

Impedance data between 150 °C and 250 °C, reveal that the conductivity of bulk is three orders of magnitude higher than the grain boundary conductivity. This is a hint that after Ultrafast High-temperature Sintering and before a heat treatment, the electrolyte conductivity is limited by the grain boundary contribution. Fig. 6 reports the grain boundary and bulk conductivities in the 100 °C–250 °C temperature range for both conventional sintering sample and UHS. The activation energy for transport through bulk is lower that for transport through grain boundaries. Moreover, while bulk transport properties are similar for the two sintering processes, grain boundaries activation energy is slightly different. The value of activation energy for bulk transport for UHS is $E_{a,bulk} = 0.60 \pm 0.01$ eV, which is consistent with C.S. and with values for analogous material reported in Ref. [11]. Activation energy for grain boundary transport is higher than that of the bulk. The value is $E_{a,g.b.} = 0.81 \pm 0.04$ eV. Grain boundaries thickness calculated from impedance data with a brick-layer model [10], ranges from 12.4 nm to 16.4 nm in the 150 °C and 250 °C, whereas for conventional sintering ranges from 2.9 nm to 3.6 nm (cfr [9]).

The material processed in this study exploits a total conductivity of 1.5 mS cm^{-1} at 500 °C and of 11 mS cm^{-1} at 750 °C (Fig. 5). The magnitude of the bulk conductivities for proton transport agrees with materials obtained with conventional sintering as reported in Fig. 7 and summarized in Table 2, with an activation energy of 0.72 eV. These values show that a fine microstructure with a correct stoichiometry of $BaCe_{0.65}Zr_{0.20}Y_{0.15}O_{3-\delta}$ electrolyte can be achieved by means of the UHS process.

4. Conclusions

A novel approach for the densification of solid oxide electrolyte was successfully applied to $BaCe_{0.65}Zr_{0.20}Y_{0.15}O_{3-\delta}$. UHS technique, implemented in this work, allowed the sintering to 95% dense BCZY sample in few seconds with an energy consumption of about 200 kJ g^{-1}. SEM and

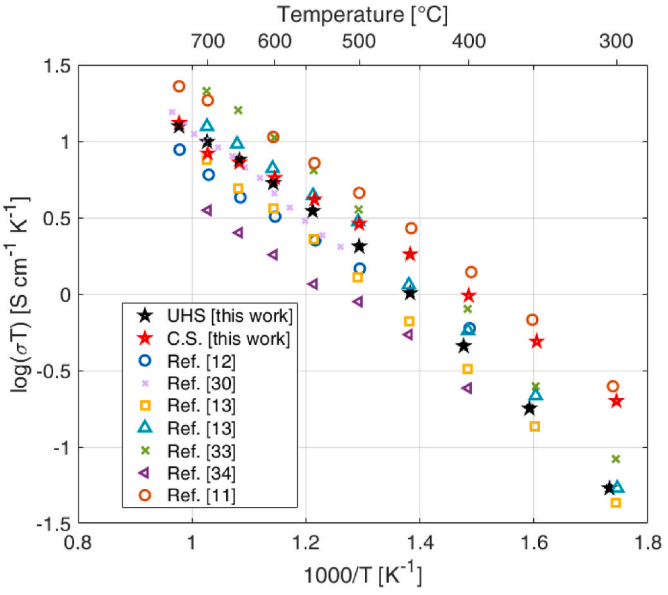

Fig. 7. Comparison of Arrhenius plots from this study and conventional sintering processes.

Table 2
Comparison of conductivities, process and sintering conditions from literature.

Material	Membrane conductivity [10^{-2} S cm^{-1}]	Process (temperature, time)	Conditions	Ref.
$BaCe_{0.65}Zr_{0.2}Y_{0.15}0_{3-\delta}$	1.02	UHS (1500 °C, 20 s)	wet H_2, 700 °C	This work
$BaCe_{0.65}Zr_{0.2}Y_{0.15}0_{3-\delta}$	0.92	Conventional sintering (1450 °C, 10 h)	wet H_2, 700 °C	This work
$BaCe_{0.65}Zr_{0.2}Y_{0.15}0_{3-\delta}$	1.9	Conventional sintering (1450 °C, 10 h)	wet H_2, 700 °C (P_{H2O} = 0.5 bar)	[11]
$BaCe_{0.7}Zr_{0.1}Y_{0.2}0_{3-\delta}$	0.78	Conventional sintering (1400 °C)	wet H_2, 700 °C	[13]
$BaCe_{0.7}Zr_{0.1}Y_{0.2}0_{3-\delta}$	1.28	Microwave furnace (1200 °C, 2h)	wet H_2, 700 °C	[13]
$BaCe_{0.7}Zr_{0.2}Y_{0.1}0_{3-\delta}$	2.17	Conventional sintering (1500 °C, 6 h)	wet H_2, 700 °C	[33]
$BaCe_{0.7}Zr_{0.1}Y_{0.2}0_{3-\delta}$	0.36	Conventional sintering (1350 °C, 6 h)	wet H_2, 700 °C	[34]
$BaCe_{0.6}Zr_{0.2}Y_{0.2}0_{3-\delta}$	1.03	Conventional sintering (1450 °C, 5 h)	wet air, 700 °C	[30]
$BaCe_{0.7}Zr_{0.2}Y_{0.1}0_{3-\delta}$	2.03	Conventional sintering (1550 °C, 10 h)	wet H_2, 700 °C	[35]
$BaCe_{0.4}Zr_{0.4}Y_{0.2}0_{3-\delta}$	1.14	Two-step sintering (1550 °C, 5 min–1450 °C 105 h)	wet air, 600 °C	[36]
$BaCe_{0.8}Zr_{0.1}Y_{0.1}0_{3-\delta}$	0.18	Cold sintering (180 °C, 30 min)	dry atmosphere, 700 °C	[37]
$BaCe_{0.8}Zr_{0.1}Y_{0.1}0_{3-\delta}$	2.30	Cold sintering + annealing (180 °C, 30 min–1200 °C, 10 h)	dry atmosphere, 700 °C	[37]
$BaCe_{0.7}In_{0.1}Y_{0.2}O_{3-\delta}$	1.4	Spark plasma sintering (1450 °C, 3 min)	wet air, 700 °C	[38]
$BaCe_{0.5}Zr_{0.3}Y_{0.2}0_{3-\delta}$	0.62	Conventional sintering (1360 °C)	wet air, 700 °C	[12]

XRD analyses confirmed the densification and the crystalline phase. Moreover, no Ba deficiency was evident. A total conductivity of 11 mS cm^{-1} was achieved at 750 °C, which is in accordance with conventional sintering techniques.

The short time and low energy used in this sintering method, together with the simple setup, open the possibility to easily study a variety of compositions.

CRediT authorship contribution statement

Andrea Turino: Investigation, Formal analysis, Data curation. **Alberto Ferrario:** Writing – review & editing, Writing – original draft, Methodology, Formal analysis, Data curation. **Stefano Fasolin:** Writing – review & editing, Investigation, Data curation. **Jacopo Isopi:** Writing – review & editing, Investigation. **Filippo Agresti:** Writing – review & editing, Formal analysis. **Simona Barison:** Writing – review & editing. **Stefano Boldrini:** Writing – review & editing, Methodology.

Declaration of competing interest

The authors declare that they have no known competing financial interests or personal relationships that could have appeared to influence the work reported in this paper.

Acknowledgement

This work has been partially founded by the 'Italian Energy Materials Acceleration Platform' project within the CNR-ENEA Agreement for Mission Innovation.

References

[1] G. Min, S. Choi, J. Hong, A review of solid oxide steam-electrolysis cell systems: thermodynamics and thermal integration, Appl. Energy 328 (2022) 120145, https://doi.org/10.1016/j.apenergy.2022.120145.
[2] E. Ivers-Tiffée, A. Weber, D. Herbstritt, Materials and technologies for SOFC-components, J. Eur. Ceram. Soc. 21 (2001) 1805–1811, https://doi.org/10.1016/S0955-2219(01)00120-0.
[3] D.A. Medvedev, J.G. Lyagaeva, E.V. Gorbova, A.K. Demin, P. Tsiakaras, Advanced materials for SOFC application: strategies for the development of highly conductive and stable solid oxide proton electrolytes, Prog. Mater. Sci. 75 (2016) 38–79, https://doi.org/10.1016/j.pmatsci.2015.08.001.
[4] T.K. Maiti, J. Majhi, S.K. Maiti, J. Singh, P. Dixit, T. Rohilla, S. Ghosh, S. Bhushan, S. Chattopadhyay, Zirconia- and ceria-based electrolytes for fuel cell applications: critical advancements toward sustainable and clean energy production, Environ. Sci. Pollut. Control Ser. 29 (2022) 64489–64512, https://doi.org/10.1007/s11356-022-22087-9.
[5] L. Mathur, Y. Namgung, H. Kim, S.-J. Song, Recent progress in electrolyte-supported solid oxide fuel cells: a review, J. Korean Ceram. Soc. 60 (2023) 614–636, https://doi.org/10.1007/s43207-023-00296-3.
[6] M. Biesuz, T.H. de Beauvoir, E.D. Bona, M. Cassetta, C. Manière, V.M. Sglavo, C. Estournès, Ultrafast high-temperature sintering (UHS) vs. conventional sintering of 3YSZ: microstructure and properties, J. Eur. Ceram. Soc. 44 (2024) 4741–4750, https://doi.org/10.1016/j.jeurceramsoc.2024.01.064.
[7] S. Wienströer, H.-D. Wiemhöfer, Investigation of the influence of zirconium substitution on the properties of neodymium-doped barium cerates, Solid State Ionics 101–103 (1997) 1113–1117, https://doi.org/10.1016/S0167-2738(97)00163-X.
[8] K.D. Kreuer, Proton-conducting oxides, Annu. Rev. Mater. Res. 33 (2003) 333–359, https://doi.org/10.1146/annurev.matsci.33.022802.091825.
[9] K.H. Ryu, S.M. Haile, Chemical stability and proton conductivity of doped BaCeO3–BaZrO3 solid solutions, Solid State Ionics 125 (1999) 355–367, https://doi.org/10.1016/S0167-2738(99)00196-4.
[10] S.M. Haile, G. Staneff, K.H. Ryu, Non-stoichiometry, grain boundary transport and chemical stability of proton conducting perovskites, J. Mater. Sci. 36 (2001) 1149–1160, https://doi.org/10.1023/A:1004877708871.
[11] S. Barison, M. Battagliarin, T. Cavallin, S. Daolio, L. Doubova, M. Fabrizio, C. Mortalò, S. Boldrini, R. Gerbasi, Barium non-stoichiometry role on the properties of Ba1+xCe0.65Zr0.20Y0.15O3–δ proton conductors for IT-SOFCs, Fuel Cell. 8 (2008) 360–368, https://doi.org/10.1002/fuce.200800021.
[12] M. Hakim, J.H. Joo, C.-Y. Yoo, B.-K. Kim, J.H. Yu, Enhanced chemical stability and sinterability of refined proton-conducting perovskite: case study of BaCe0.5Zr0.3Y0.2O3−δ, J. Eur. Ceram. Soc. 35 (2015) 1855–1863, https://doi.org/10.1016/j.jeurceramsoc.2014.11.033.
[13] X. Xu, L. Bi, X.S. Zhao, Highly-conductive proton-conducting electrolyte membranes with a low sintering temperature for solid oxide fuel cells, J. Membr. Sci. 558 (2018) 17–25, https://doi.org/10.1016/j.memsci.2018.04.037.
[14] C. Wang, W. Ping, Q. Bai, H. Cui, R. Hensleigh, R. Wang, A.H. Brozena, Z. Xu, J. Dai, Y. Pei, C. Zheng, G. Pastel, J. Gao, X. Wang, H. Wang, J.-C. Zhao, B. Yang, X. Zheng, J. Luo, Y. Mo, B. Dunn, L. Hu, A general method to synthesize and sinter bulk ceramics in seconds, Science 368 (2020) 521–526, https://doi.org/10.1126/science.aaz7681.
[15] J. Dong, V. Pouchly, M. Biesuz, V. Tyrpekl, M. Vilémová, M. Kermani, M. Reece, C. Hu, S. Grasso, Thermally-insulated ultra-fast high temperature sintering (UHS) of zirconia: a master sintering curve analysis, Scripta Mater. 203 (2021) 114076, https://doi.org/10.1016/j.scriptamat.2021.114076.
[16] Q. Li, H. Du, X. Zhao, F. Zhao, Y. Zhang, X. Hu, X. Du, Densification and microstructure evolution of NaNbO3 ceramic via ultrafast high-temperature sintering, Ceram. Int. 50 (2024) 18907–18914, https://doi.org/10.1016/j.ceramint.2024.02.378.
[17] D. Wang, X. Wang, C. Xu, Z. Fu, J. Zhang, Densification mechanism of the ultra-fast sintering dense alumina, AIP Adv. 10 (2020) 25223, https://doi.org/10.1063/1.5119030.
[18] F. Ye, F. Meng, T. Luo, H. Qi, Ultrafast high-temperature sintering of high-entropy (La0.2Nd0.2Sm0.2Eu0.2Gd0.2)2Hf2O7 ceramics with fluorite structure, Ceram. Int. 48 (2022) 35649–35654, https://doi.org/10.1016/j.ceramint.2022.09.041.
[19] H.-Z. Shen, R.-F. Guo, P. Shen, Efficient synthesis and densification of MgAl2O4 ceramics: combining reactive cold sintering with ultrafast high-temperature sintering, J. Eur. Ceram. Soc. 44 (2024) 4816–4821, https://doi.org/10.1016/j.jeurceramsoc.2024.01.077.

[20] S. Bhandari, C. Manière, F. Sedona, E.D. Bona, V.M. Sglavo, P. Colombo, L. Fambri, M. Biesuz, G. Franchin, Ultra-rapid debinding and sintering of additively manufactured ceramics by ultrafast high-temperature sintering, J. Eur. Ceram. Soc. 44 (2024) 328–340, https://doi.org/10.1016/j.jeurceramsoc.2023.08.040.

[21] C. Wang, W. Zhong, W. Ping, Z. Lin, R. Wang, J. Dai, M. Guo, W. Xiong, J.-C. Zhao, L. Hu, Rapid synthesis and sintering of metals from powders, Adv. Sci. 8 (2021) 2004229, https://doi.org/10.1002/advs.202004229.

[22] R.-X. Luo, M. Kermani, Z.-L. Guo, J. Dong, C.-F. Hu, F. Zuo, S. Grasso, B.-B. Jiang, G.-L. Nie, Z.-Q. Yan, Q. Wang, Y.-L. Gan, F.-P. He, H.-T. Lin, Ultrafast high-temperature sintering of silicon nitride: a comparison with the state-of-the-art techniques, J. Eur. Ceram. Soc. 41 (2021) 6338–6345, https://doi.org/10.1016/j.jeurceramsoc.2021.06.021.

[23] S. Boldrini, A. Ferrario, S. Fasolin, A. Miozzo, S. Barison, Ultrafast high-temperature sintering and thermoelectric properties of n-doped Mg2Si, Nanotechnology 34 (2023) 155601, https://doi.org/10.1088/1361-6528/acb15a.

[24] A. Alemayehu, M. Biesuz, K.Y. Javan, A. Tkach, P.M. Vilarinho, V.M. Sglavo, V. Tyrpekl, Ultrafast high-temperature sintering of gadolinia-doped ceria, J. Eur. Ceram. Soc. 43 (2023) 4837–4843, https://doi.org/10.1016/j.jeurceramsoc.2023.04.025.

[25] Q. Pan, D. Huan, Z. Jin, X. Liu, W. Xiang, X. Kong, B. Feng, Z. Wang, M. Dai, R. Peng, Z. Zhan, C. Chen, C. Wang, A new composite proton conductor as a high-performance electrolyte toward low-temperature protonic ceramic cells, ACS Energy Lett. 9 (2024) 2286–2292, https://doi.org/10.1021/acsenergylett.3c02590.

[26] F. Zuo, Q. Wang, Z.-Q. Yan, M. Kermani, S. Grasso, G.-L. Nie, B.-B. Jiang, F.-P. He, H.-T. Lin, L.-G. Wang, Upscaling Ultrafast High-Temperature Sintering (UHS) to consolidate large-sized and complex-shaped ceramics, Scripta Mater. 221 (2022) 114973, https://doi.org/10.1016/j.scriptamat.2022.114973.

[27] S. Barison, M. Battagliarin, T. Cavallin, L. Doubova, M. Fabrizio, C. Mortalò, S. Boldrini, L. Malavasi, R. Gerbasi, High conductivity and chemical stability of BaCe1−x−yZrxYyO3−δ proton conductors prepared by a sol–gel method, J. Mater. Chem. 18 (2008) 5120–5128, https://doi.org/10.1039/B808344D.

[28] M. Biesuz, L. Karacasulu, C. Vakifahmetoglu, V.M. Sglavo, On the temperature measurement during ultrafast high-temperature sintering (UHS): shall we trust metal-shielded thermocouples? J. Eur. Ceram. Soc. (2023) https://doi.org/10.1016/j.jeurceramsoc.2023.11.061.

[29] J. Wu, Y. Lin, M. Kermani, C. Hu, S. Grasso, Ultra-fast high temperature sintering (UHS) of Li1.5Al0.5Ge1.5P3O12 electrolyte: a rationalization of the heating schedule, Ceram. Int. 48 (2022) 6356–6362, https://doi.org/10.1016/j.ceramint.2021.11.178.

[30] J. Lagaeva, D. Medvedev, A. Demin, P. Tsiakaras, Insights on thermal and transport features of BaCe0.8−xZrxY0.2O3−δ proton-conducting materials, J. Power Sources 278 (2015) 436–444, https://doi.org/10.1016/j.jpowsour.2014.12.024.

[31] J.F. Basbus, M.D. Arce, F.R. Napolitano, H.E. Troiani, J.A. Alonso, M.E. Saleta, M. A. González, G.J. Cuello, M.T. Fernández-Díaz, M.P. Sainz, N. Bonanos, C. E. Jimenez, L. Giebeler, S.J.A. Figueroa, A. Caneiro, A.C. Serquis, L.V. Mogni, Revisiting the crystal structure of BaCe0.4Zr0.4Y0.2O3−δ proton conducting perovskite and its correlation with transport properties, ACS Appl. Energy Mater. 3 (2020) 2881–2892, https://doi.org/10.1021/acsaem.9b02498.

[32] T. Miruszewski, K. Dzierzgowski, P. Winiarz, S. Wachowski, A. Mielewczyk-Gryń, M. Gazda, Hebb–Wagner polarization method for determining the oxygen ion conductivity in barium cerate-zirconate, J. Mater. Chem. A 10 (2022) 7218–7227, https://doi.org/10.1039/D1TA10916B.

[33] K. Yang, J.X. Wang, Y.J. Xue, M.S. Wang, C.R. He, Q. Wang, H. Miao, W.G. Wang, Synthesis, sintering behavior and electrical properties of Ba(Zr0.1Ce0.7Y0.2)O3−δ and Ba(Zr0.1Ce0.7Y0.1Yb0.1)O3−δ proton conductors, Ceram. Int. 40 (2014) 15073–15081, https://doi.org/10.1016/j.ceramint.2014.06.115.

[34] L. Yang, C. Zuo, M. Liu, High-performance anode-supported Solid Oxide Fuel Cells based on Ba(Zr0.1Ce0.7Y0.2)O3−δ (BZCY) fabricated by a modified co-pressing process, J. Power Sources 195 (2010) 1845–1848, https://doi.org/10.1016/j.jpowsour.2009.10.018.

[35] C. Zuo, S. Zha, M. Liu, M. Hatano, M. Uchiyama, Ba(Zr0.1Ce0.7Y0.2)O3–δ as an electrolyte for low-temperature solid-oxide fuel cells, Adv. Mater. 18 (2006) 3318–3320, https://doi.org/10.1002/adma.200601366.

[36] G.S. Reddy, R. Bauri, A novel route to enhance the sinterability and its effect on microstructure, conductivity and chemical stability of BaCe0.4Zr0.4Y0.2O3-δ proton conductors, Mater. Chem. Phys. 216 (2018) 250–259, https://doi.org/10.1016/j.matchemphys.2018.05.023.

[37] K. Thabet, A.L.G.L. Salle, E. Quarez, O. Joubert, High performance dense proton ceramic electrolyte material obtained by cold sintering process, ECS Trans. 91 (2019) 983, https://doi.org/10.1149/09101.0983ecst.

[38] S.A. Sergiienko, V.A. Kolotygin, N.D. Shcherban, S.M. Filonenko, D. O. Moskovskikh, A.A. Nepapushev, D.I. Arkhipov, O.B. Tursunov, Structure and transport properties of the spark plasma sintered barium cerate based proton conductor, Ceram. Int. 43 (2017) 14905–14914, https://doi.org/10.1016/j.ceramint.2017.08.007.